Chapter 21
Experimental Modal Analysis of Nonlinear Structures Using Broadband Data

J.P. Noël, L. Renson, C. Grappasonni, and G. Kerschen

Abstract The objective of the present paper is to develop a rigorous identification methodology of nonlinear normal modes (NNMs) of engineering structures. This is achieved by processing experimental measurements collected under broadband forcing. The use of such a type of forcing signal allows to excite multiple NNMs simultaneously and, in turn, to save testing time. A two-step methodology integrating nonlinear system identification and numerical continuation of periodic solutions is proposed for the extraction of the individual NNMs from broadband input and output data. It is demonstrated using a numerical cantilever beam possessing a cubic nonlinearity at its free end. The proposed methodology can be viewed as a nonlinear generalization of the phase separation techniques routinely utilized for experimental modal analysis of linear structures. The paper ends with a comparison between this new nonlinear phase separation technique and a previously-developed nonlinear phase resonance method.

Keywords Nonlinear normal modes • Experimental data • Broadband excitation • Nonlinear system identification • Numerical continuation

21.1 Introduction

Experimental modal analysis of linear engineering structures is now well-established and mature [1]. It is routinely practiced in industry, in particular during on-ground certification of aircraft and spacecraft structures [2–4], using two specific approaches, namely phase resonance and phase separation methods. Phase resonance testing, also known as force appropriation, consists in exciting the normal modes of interest one at a time using a multipoint sine forcing at the corresponding natural frequency [5]. Conversely, in phase separation testing, several normal modes are excited simultaneously using either broadband or swept-sine forcing, and are subsequently identified using appropriate linear system identification techniques [6, 7].

The existence of nonlinear behavior in dynamic testing, at least in certain regimes of motion, is today a challenge the structural engineer is more and more frequently confronted with. In this context, the development of a nonlinear counterpart to experimental modal analysis would be extremely beneficial. An interesting approach is the so-called nonlinear resonant decay method introduced by Wright and co-workers [8, 9]. In this approach, a burst of a sine wave is applied to the structure at the undamped natural frequency of a normal mode, and enables small groups of modes coupled by nonlinear forces to be excited. A nonlinear curve fitting in modal space is then carried out using the restoring force surface method. The identification of modes from multimodal nonlinear responses has also been attempted in the past few years. For that purpose, advanced signal processing techniques have been utilized, including the empirical mode decomposition [10–12], time-frequency analysis tools [13] and machine learning algorithms [14]. Multimodal identification relying on the synthesis of frequency response functions using individual mode contributions has been proposed in [15, 16]. The difficulty with these approaches is the absence of superposition principle in nonlinear dynamics, preventing the response of a nonlinear system from being decomposed into the sum of different modal responses.

In the present study, we adopt the framework offered by the theory of nonlinear normal modes (NNMs) to perform experimental nonlinear modal analysis. The concept of normal modes was generalized to nonlinear systems by Rosenberg in the 1960s [17, 18] and by Shaw and Pierre in the 1990s [19]. NNMs possess a clear conceptual relation with the classical linear normal modes (LNMs) of vibration, while they provide a solid mathematical tool for interpreting a wide

J.P. Noël (✉) • L. Renson • C. Grappasonni • G. Kerschen
Space Structures and Systems Laboratory (S3L), Aerospace and Mechanical Engineering Department, University of Liège, Liège, Belgium
e-mail: jp.noel@ulg.ac.be; l.renson@ulg.ac.be; chiara.grappasonni@ulg.ac.be; g.kerschen@ulg.ac.be

G. Kerschen (ed.), *Nonlinear Dynamics, Volume 1*, Conference Proceedings of the Society for Experimental Mechanics Series, DOI 10.1007/978-3-319-15221-9_21

class of nonlinear dynamic phenomena, see, e.g., [20–23]. There now exist effective algorithms for their computation from mathematical models [24–27]. For instance, the NNMs of full-scale aircraft and spacecraft structures and of a turbine bladed disk were computed in [28–30], respectively.

A nonlinear phase resonance method exploiting the NNM concept was first proposed in [31], and was validated experimentally in [32]. Following the philosophy of force appropriation and relying on a nonlinear generalization of the phase lag quadrature criterion, this nonlinear phase resonance method excites the targeted NNMs one at a time using a multipoint, multiharmonic sine forcing. The energy-dependent frequency and modal curve of each NNM are then extracted directly from the experimental time series by virtue of the invariance principle of nonlinear oscillations. Applications of nonlinear phase resonance testing to moderately complex experimental structures were recently reported in the technical literature, in the case of a steel frame in [33] and of a circular perforated plate in [34].

The objective of the present paper is to develop a rigorous identification methodology of NNMs by processing experimental measurements collected under broadband forcing. The use of such a type of forcing signal allows, in contrast with a phase resonance approach, to excite multiple NNMs simultaneously and, in turn, to save testing time. A two-step methodology integrating nonlinear system identification and numerical continuation of periodic solutions is proposed for the extraction of the individual NNMs from broadband input and output data. More specifically, the frequency-domain nonlinear subspace identification (FNSI) method, introduced in [35], is first applied to measured data to derive an undamped experimental model of the nonlinear structure of interest, assuming an accurate characterization of the nonlinearities. Secondly, a numerical algorithm implementing pseudo-arclength continuation [25] is exploited to compute the NNMs of the structure based on the experimentally-derived model.

The paper is organized as follows. The fundamental properties of NNMs defined as periodic solutions of the underlying undamped system are briefly reviewed in Sect. 21.2. The existing nonlinear phase resonance method introduced in [31] is also described. In Sect. 21.3, the two building blocks of the proposed NNM identification methodology, namely the FNSI method and the pseudo-arclength continuation algorithm, are presented in detail. The methodology is demonstrated in Sect. 21.4 using numerical experiments on a cantilever beam possessing a cubic nonlinearity at its free end. Since it can be viewed as a nonlinear generalization of linear phase separation techniques, the proposed methodology is also compared in Sect. 21.5 with the previously-developed nonlinear phase resonance method. The conclusions of the study are finally summarized in Sect. 21.6.

21.2 Brief Review of Nonlinear Normal Modes (NNMs) and Identification Using Phase Resonance

In this work, an extension of Rosenberg's definition of a NNM is considered [23]. Specifically, a NNM is defined as a nonnecessarily synchronous, periodic motion of the undamped, unforced system

$$\mathbf{M}\,\ddot{\mathbf{q}}(t) + \mathbf{K}\,\mathbf{q}(t) + \mathbf{f}(\mathbf{q}(t)) = 0 \tag{21.1}$$

where $\mathbf{M}$ and $\mathbf{K} \in \mathbb{R}^{n_p \times n_p}$ are the mass and linear stiffness matrices, respectively; $\mathbf{q} \in \mathbb{R}^{n_p}$ is the generalized displacement vector; $\mathbf{f}(\mathbf{q}(t)) \in \mathbb{R}^{n_p}$ is the nonlinear restoring force vector encompassing elastic terms only; n_p is the number of degrees of freedom (DOFs) of the system. This definition of a NNM may appear to be restrictive in the case of nonconservative systems. However, as shown in [23], the topology of the underlying conservative NNMs of a system yields considerable insight into its damped dynamics.

Because a salient feature of nonlinear systems is the frequency-energy dependence of their oscillations, the depiction of NNMs is conveniently realized in a frequency-energy plot (FEP). A NNM motion in a FEP is represented by a point associated with the fundamental frequency of the periodic motion, and with the total conserved energy accompanying the motion. A branch in a FEP details the complete frequency-energy dependence of the considered mode. By way of illustration, the FEP of the two-DOF system described by the equations

$$\begin{aligned} \ddot{q}_1 + (2\,q_1 - q_2) + 0.5\,q_1^3 &= 0 \\ \ddot{q}_2 + (2\,q_2 - q_1) &= 0 \end{aligned} \tag{21.2}$$

is plotted in Fig. 21.1. The plot consists of two branches corresponding to the in-phase and out-of-phase synchronous NNMs of the system. These fundamental NNMs are the direct nonlinear extension of the corresponding LNMs. The nonlinear modal

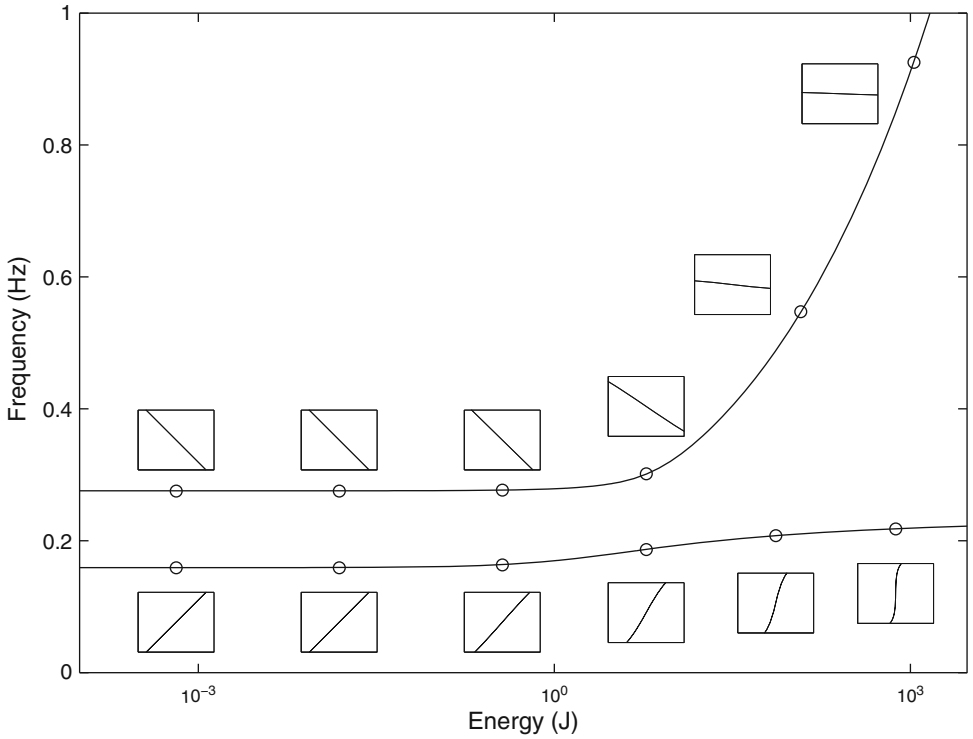

Fig. 21.1 FEP of the two-DOF system described by Eq. (21.2). NNM motions depicted in displacement space are *inset*. The horizontal and vertical axes in these plots are the displacements of the first and second DOF of the system, respectively

parameters, i.e. the frequencies of oscillation and the modal curves, are found to depend markedly on the energy. In particular, the frequency of the two fundamental NNMs increases with the energy level, revealing the hardening characteristic of the cubic stiffness nonlinearity in the system.

The absence of superposition principle in nonlinear dynamics renders by no means straightforward the identification of NNMs from broadband measurements (see Sect. 21.3). However, two essential properties of linear systems are preserved in the presence of nonlinearity. First, forced resonances of nonlinear systems occur in the neighborhood of NNMs [20]. Second, NNMs obey the invariance principle, which states that if the motion is initiated on one specific NNM, the remaining NNMs are quiescent for all time [19].

These two properties were exploited in [31] to develop a rigorous nonlinear phase resonance method based on sine data. The procedure comprises two steps, as illustrated in Fig. 21.2. During the first step, termed NNM force appropriation, the system is excited to induce a single-NNM motion at a prescribed energy level. This step is facilitated by a generalized phase lag quadrature criterion applicable to nonlinear systems [31]. This criterion asserts that a structure vibrates according to an underlying conservative NNM if the measured responses possess, for all harmonics, a phase difference of 90° with respect to the excitation. The second step of the procedure, termed NNM free-decay identification, turns off the excitation to track the energy dependence of the appropriated NNM. The associated modal parameters are extracted directly from the free damped system response through time-frequency analysis. This nonlinear phase resonance method was found to be highly accurate but, as linear phase resonance testing, very time-consuming. In addition, to reach the neighborhood of the resonance where a specific NNM lives may require a cumbersome trial-and-error approach to deal with the shrinking basins of attraction along forced resonance peaks. The methodology described in the next section precisely addresses these two issues.

21.3 Identification Methodology of Nonlinear Normal Modes (NNMs) Under Broadband Forcing

The methodology proposed in this paper for the identification of NNMs using broadband measurements is presented in Fig. 21.3. It comprises two major steps. The first step consists in processing acquired input and output data to construct an experimental undamped model of the nonlinear structure of interest. In the present study, this model takes the form of a set of first-order equations in the state space. In a second step, the energy-dependent frequencies and modal curves of the excited NNMs are computed individually by applying a numerical continuation algorithm to the undamped model equations.

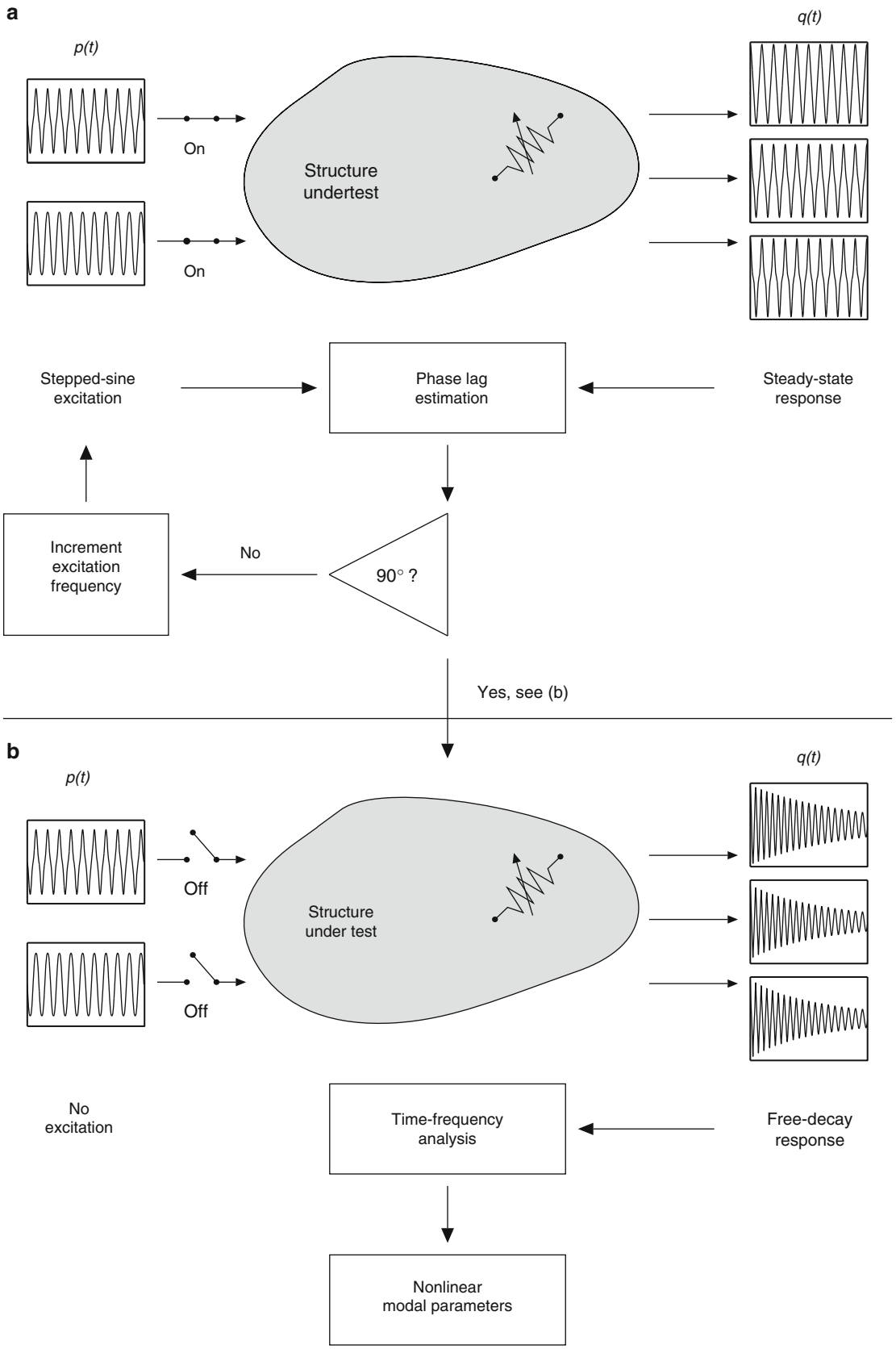

Fig. 21.2 Experimental modal analysis of nonlinear systems using a nonlinear phase resonance method [31]. (**a**) NNM force appropriation; (**b**) NNM free-decay identification

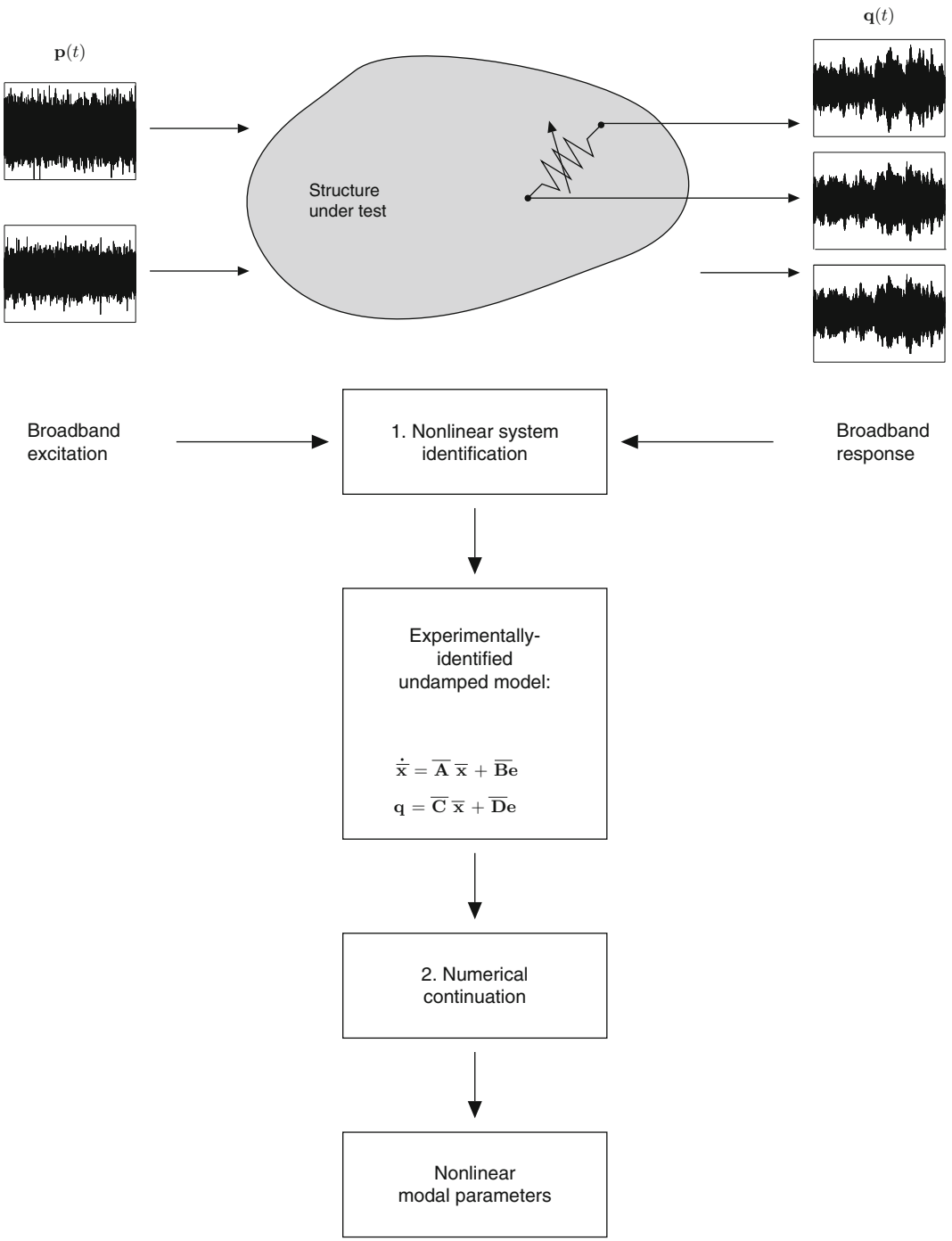

Fig. 21.3 Proposed methodology for the identification of NNMs based on broadband measurements. It comprises two major steps, namely nonlinear system identification and numerical continuation

Section 21.3.1 describes how the experimental state-space model can be derived in the frequency domain by employing the FNSI method. Section 21.3.2 next outlines one existing algorithm, based on pseudo-arclength continuation, for the computation of NNMs defined as periodic solutions.

21.3.1 Experimental Identification of an Undamped Nonlinear State-Space Model

In the present section, the experimental extraction of a nonlinear undamped model of the structure under test is achieved by means of a subspace identification technique, termed FNSI method [35]. The FNSI method is capable of deriving models of nonlinear vibrating systems directly from measured data, and without resorting to a preexisting numerical model, e.g. a finite element model. It is applicable to multi-input, multi-output structures with high damping and high modal density, and makes no assumption as to the importance of nonlinearity in the measured dynamics [36, 37]. It will also be shown in this section that the application of the FNSI method requires the measurement of the applied forces together with the dynamic responses throughout the structure, including at the driving points and across the nonlinear components.

21.3.1.1 Nonlinear Model Equations in the Physical Space

The vibrations of damped nonlinear systems obey Newton's second law of dynamics

$$\mathbf{M}\,\ddot{\mathbf{q}}(t) + \mathbf{C}_v\,\dot{\mathbf{q}}(t) + \mathbf{K}\,\mathbf{q}(t) + \mathbf{f}(\mathbf{q}(t), \dot{\mathbf{q}}(t)) = \mathbf{p}(t) \tag{21.3}$$

where $\mathbf{C}_v \in \mathbb{R}^{n_p \times n_p}$ is the linear viscous damping matrix; $\mathbf{p}(t) \in \mathbb{R}^{n_p}$ is the generalized external force vector; $\mathbf{f}(\mathbf{q}(t), \dot{\mathbf{q}}(t)) \in \mathbb{R}^{n_p}$ is the nonlinear restoring force vector encompassing elastic and dissipative terms. Note that Eq. (21.3) represents the damped and forced generalization of Eq. (21.1). The nonlinear restoring force term in Eq. (21.3) is expressed by means of a linear combination of known basis functions $\mathbf{h}_a(\mathbf{q}(t), \dot{\mathbf{q}}(t))$ as

$$\mathbf{f}(\mathbf{q}(t), \dot{\mathbf{q}}(t)) = \sum_{a=1}^{s} c_a\,\mathbf{h}_a(\mathbf{q}(t), \dot{\mathbf{q}}(t)). \tag{21.4}$$

In this sum, the coefficients c_a associated with the nonlinear basis functions $\mathbf{h}_a(\mathbf{q}(t), \dot{\mathbf{q}}(t))$ play a role similar to the linear stiffness and viscous damping coefficients contained in the matrices $\mathbf{K}$ and $\mathbf{C}_v$ in Eq. (21.3), respectively. Note that the total number of basis functions s introduced in the model may be larger than the number of physical nonlinearity sources in the system, as multiple model terms are generally required to capture the behavior of a single nonlinear component.

Given measurements of $\mathbf{p}(t)$ and $\mathbf{q}(t)$ or its derivatives, and an appropriate selection of the functionals $\mathbf{h}_a(t)$, the application of the FNSI method in the present study aims at constructing a state-space model describing the undamped dynamics associated with Eq. (21.3). Models in the state space are appealing because of their intrinsic capability to represent systems with multiple inputs and outputs. They can also be effectively utilized to predict the response of the system under a given forcing function by direct time integration (see Sect. 21.3.2).

21.3.1.2 Feedback Interpretation and State-Space Model Equations

The FNSI approach builds on a block-oriented interpretation of nonlinear structural dynamics, which sees nonlinearities as a feedback into the linear system in the forward loop [38], as illustrated in Fig. 21.4. This interpretation boils down to moving the nonlinear internal forces in Eq. (21.3) to the right-hand side, and viewing them as additional external forces applied to the underlying linear structure, that is,

$$\mathbf{M}\,\ddot{\mathbf{q}}(t) + \mathbf{C}_v\,\dot{\mathbf{q}}(t) + \mathbf{K}\,\mathbf{q}(t) = \mathbf{p}(t) - \sum_{a=1}^{s} c_a\,\mathbf{h}_a(\mathbf{q}(t), \dot{\mathbf{q}}(t)). \tag{21.5}$$

Without loss of generality, it is assumed in this section that the structural response is measured in terms of generalized displacements. Defining the state vector $\mathbf{x} = \left(\mathbf{q}^T \;\; \dot{\mathbf{q}}^T\right)^T \in \mathbb{R}^{n_s}$, where $n_s = 2\,n_p$ is the dimension of the state space and T the matrix transpose, Eq. (21.5) is recast into the set of first-order equations

$$\begin{cases} \dot{\mathbf{x}}(t) = \mathbf{A}\,\mathbf{x}(t) + \mathbf{B}\,\mathbf{e}(t) \\ \mathbf{q}(t) = \mathbf{C}\,\mathbf{x}(t) + \mathbf{D}\,\mathbf{e}(t) \end{cases} \tag{21.6}$$

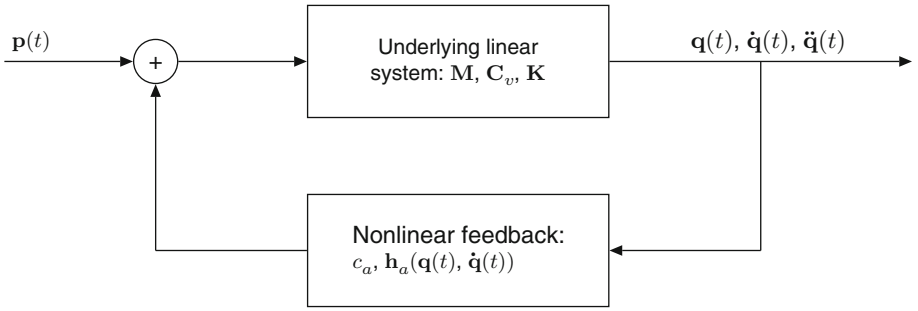

Fig. 21.4 Feedback interpretation of nonlinear structural dynamics [38]

where the vector $\mathbf{e} \in \mathbb{R}^{(s+1)\,n_p}$, termed *extended input vector*, concatenates the external forces $\mathbf{p}(t)$ and the nonlinear basis functions $\mathbf{h}_a(t)$. The matrices $\mathbf{A} \in \mathbb{R}^{n_s \times n_s}$, $\mathbf{B} \in \mathbb{R}^{n_s \times (s+1)\,n_p}$, $\mathbf{C} \in \mathbb{R}^{n_p \times n_s}$ and $\mathbf{D} \in \mathbb{R}^{n_p \times (s+1)\,n_p}$ are the state, extended input, output and direct feedthrough matrices, respectively. State-space and physical-space matrices correspond through the relations

$$\mathbf{A} = \begin{pmatrix} \mathbf{0}^{n_p \times n_p} & \mathbf{I}^{n_p \times n_p} \\ -\mathbf{M}^{-1}\,\mathbf{K} & -\mathbf{M}^{-1}\,\mathbf{C}_v \end{pmatrix} ; \mathbf{B} = \begin{pmatrix} \mathbf{0}^{n_p \times n_p} & \mathbf{0}^{n_p \times n_p} & \mathbf{0}^{n_p \times n_p} & \dots & \mathbf{0}^{n_p \times n_p} \\ \mathbf{M}^{-1} & -c_1\,\mathbf{M}^{-1} & -c_2\,\mathbf{M}^{-1} & \dots & -c_s\,\mathbf{M}^{-1} \end{pmatrix}$$

$$\mathbf{C} = \begin{pmatrix} \mathbf{I}^{n_p \times n_p} & \mathbf{0}^{n_p \times n_p} \end{pmatrix} ; \mathbf{D} = \mathbf{0}^{n_p \times (s+1)\,n_p} \tag{21.7}$$

where $\mathbf{0}$ and $\mathbf{I}$ are the zero and identity matrices, respectively. It should be remarked that no identifiability condition constrains the number of measured displacements, provided that the nonlinear basis functions $\mathbf{h}_a(\mathbf{q}(t), \dot{\mathbf{q}}(t))$ can be formed from the recorded channels [35]. This implies that the nonlinear components in the structure must be instrumented on both sides in order to measure the relative displacement and velocity required in the formulation of the nonlinear basis functions $\mathbf{h}_a(\mathbf{q}(t), \dot{\mathbf{q}}(t))$, as illustrated in Fig. 21.3.

The FNSI estimation of the four system matrices $\mathbf{A}$, $\mathbf{B}$, $\mathbf{C}$ and $\mathbf{D}$ is achieved in the frequency domain using a classical subspace resolution scheme. This resolution essentially involves the reformulation of Eq. (21.6) in matrix form, and the computation of estimates of $(\mathbf{A}, \mathbf{B}, \mathbf{C}, \mathbf{D})$ through geometrical manipulations of input and output data. The interested reader is referred to [35] for a complete introduction to the theoretical and practical aspects of the FNSI method.

21.3.1.3 Conversion from State Space to Physical and Modal Space

The identified state-space model $(\mathbf{A}, \mathbf{B}, \mathbf{C}, \mathbf{D})$ can be converted into estimates of (1) the nonlinear coefficients c_a and (2) the underlying linear modal properties of the system. Linear and nonlinear system properties will prove useful in the construction of undamped state-space model equations in Sect. 21.3.1.4. They will also prove convenient to assess the quality of the identification in Sects. 21.4.1.3 and 21.4.1.4. The complexity of the conversion addressed in this subsection stems from an unknown similarity transformation of the state-space basis within which the FNSI model is derived [35]. Because the nonlinear coefficients c_a are elements of the matrix $\mathbf{B}$, they vary according to the choice of the basis in which $\mathbf{B}$ is calculated. Therefore, the estimates of c_a cannot be obtained from a direct inspection of $\mathbf{B}$.

To achieve the conversion to physical and modal space, the transfer function matrix $\mathbf{G}_s(\omega)$ associated with the state-space model is formed as

$$\mathbf{G}_s(\omega) = \mathbf{C}\left(j\omega\,\mathbf{I}^{n_s \times n_s} - \mathbf{A}\right)^{-1}\mathbf{B} + \mathbf{D} \tag{21.8}$$

where ω is the pulsation and j the imaginary unit. Matrix $\mathbf{G}_s(\omega)$ is an invariant system property with respect to any similarity transformation of the state-space basis [39]. It can be expressed in terms of the physical and modal properties of the system by substituting Eq. (21.4) into Eq. (21.3) in the frequency domain, which leads to

$$\mathbf{G}^{-1}(\omega)\mathbf{Q}(\omega) + \sum_{a=1}^{s} c_a\,\mathbf{H}_a(\omega) = \mathbf{P}(\omega) \tag{21.9}$$

where $\mathbf{G}(\omega) = \left(-\omega^2\,\mathbf{M} + j\,\omega\,\mathbf{C}_v + \mathbf{K}\right)^{-1}$ is the frequency response function (FRF) matrix of the underlying linear system, and where $\mathbf{Q}(\omega)$, $\mathbf{H}_a(\omega)$ and $\mathbf{P}(\omega)$ are the continuous Fourier transforms of $\mathbf{q}(t)$, $\mathbf{h}_a(t)$ and $\mathbf{p}(t)$, respectively. The concatenation of $\mathbf{P}(\omega)$ and $\mathbf{H}_a(\omega)$ into the extended input spectrum $\mathbf{E}(\omega)$ finally gives

$$\mathbf{Q}(\omega) = \mathbf{G}(\omega)\left[\,\mathbf{I}^{n_p\times n_p}\; -c_1\,\mathbf{I}^{n_p\times n_p}\;\ldots\;-c_s\,\mathbf{I}^{n_p\times n_p}\,\right]\mathbf{E}(\omega) = \mathbf{G}_s(\omega)\,\mathbf{E}(\omega). \tag{21.10}$$

Matrix $\mathbf{G}(\omega)$ is simply extracted using Eqs. (21.8) and (21.10) as the first n_p columns of matrix $\mathbf{G}_s(\omega)$. Subsequently, the nonlinear coefficients c_a are computed from the other columns of $\mathbf{G}_s(\omega)$ given the knowledge of $\mathbf{G}(\omega)$.

Moreover, the system damped and undamped natural frequencies, denoted ω_i and $\omega_{i,0}$, respectively, can be estimated together with the unscaled mode shape vectors $\boldsymbol{\psi}^{(i)} \in \mathbb{R}^{n_s}$ by solving the eigenvalue problem associated with the state matrix $\mathbf{A}$, that is,

$$\mathbf{A}\,\boldsymbol{\psi}^{(i)} = \lambda_i\,\boldsymbol{\psi}^{(i)},\quad i = 1,..,n_s. \tag{21.11}$$

The imaginary part $\mathcal{I}(\lambda_i)$ and the absolute value $|\lambda_i|$ of the complex eigenvalues λ_i provide the damped and undamped natural frequencies, respectively. Moreover, the state-space mode shape vectors $\boldsymbol{\psi}^{(i)}$ are converted into the corresponding physical-space modes $\tilde{\boldsymbol{\phi}}^{(i)}$ utilizing the output matrix $\mathbf{C}$ as

$$\tilde{\boldsymbol{\phi}}^{(i)} = \mathbf{C}\,\boldsymbol{\psi}^{(i)}. \tag{21.12}$$

Each mode shape vector $\tilde{\boldsymbol{\phi}}^{(i)}$ can be scaled using the residue $R_{kk}^{(i)}$ of the driving point FRF $G_{kk}(\omega)$ of the underlying linear system formulated as

$$G_{kk}(\omega) = \sum_{i=1}^{n_p} \frac{R_{kk}^{(i)}}{j\,\omega - \lambda_i} + \frac{R_{kk}^{(i)^*}}{j\,\omega - \lambda_i^*} \tag{21.13}$$

where k is the location of the excited DOF within the n_p DOFs of the structure, and where a star denotes the complex conjugate operation. Equation (21.13) is an overdetermined algebraic system of equations with n_p unknowns and as many equations as the number of processed frequency lines. The ith scaled mode shape vector at the driving point $\phi_k^{(i)}$ is finally obtained by enforcing a unit modal mass, i.e.

$$R_{kk}^{(i)} = \frac{\phi_k^{(i)}\,\phi_k^{(i)}}{2\,j\,\omega_{i,0}}, \tag{21.14}$$

while the other components of the mode shape vector $\tilde{\boldsymbol{\phi}}^{(i)}$ are scaled accordingly.

It should be noted that the mode scaling adopted in this section is rigorously valid if the linear damping mechanisms in the tested structure are proportional to the mass and stiffness distributions [40]. This assumption is compatible with the presence of weak damping. This implies that the mode shape vector at the driving point $\phi_k^{(i)}$ is real-valued in Eq. (21.14). In general, experimental mode shapes are however complex-valued. They can be enforced to be real by rotating each mode in the complex plane by an angle equal to the mean of the phase angles of the mode components, and subsequently neglecting the imaginary parts of the rotated components.

21.3.1.4 Removal of Damping Terms in the Identified State-Space Model

The removal of damping terms in the identified state-space model is necessary to allow the calculation of undamped NNMs as defined in Sect. 21.2. This is achieved in this subsection by recasting Eq. (21.6) into modal space. For that purpose, the vector of modal coordinates $\overline{\mathbf{q}}(t) \in \mathbb{R}^{n_p}$ is introduced as

$$\mathbf{q}(t) = \boldsymbol{\Phi}\,\overline{\mathbf{q}}(t) \tag{21.15}$$

where $\boldsymbol{\Phi} \in \mathbb{R}^{n_p\times n_p}$ is the matrix of the scaled mode shape vectors $\boldsymbol{\phi}^{(i)}$, and where a bar signals a vector or a matrix expressed in modal space. It is known that the projection of Eq. (21.5) into modal space yields

$$\mathbf{I}^{n_p \times n_p}\,\ddot{\overline{\mathbf{q}}}(t) + \overline{\mathbf{C}}_v\,\dot{\overline{\mathbf{q}}}(t) + \overline{\mathbf{K}}\,\overline{\mathbf{q}}(t) = \mathbf{\Phi}^T\,\mathbf{p}(t) - \sum_{a=1}^{s} c_a\,\mathbf{\Phi}^T\,\mathbf{h}_a(\mathbf{q}(t), \dot{\mathbf{q}}(t)) \tag{21.16}$$

where $\mathbf{\Phi}^T\,\mathbf{M}\,\mathbf{\Phi} = \overline{\mathbf{M}} = \mathbf{I}^{n_p \times n_p}$ since the linear mode shapes were unit-mass-scaled in the previous subsection, $\mathbf{\Phi}^T\,\mathbf{C}_v\,\mathbf{\Phi} = \overline{\mathbf{C}}_v$ and $\mathbf{\Phi}^T\,\mathbf{K}\,\mathbf{\Phi} = \overline{\mathbf{K}}$. The projected stiffness matrix $\overline{\mathbf{K}}$ is a diagonal matrix populated with the squared values of the undamped frequencies $\omega_{i,0}$, i.e. $\text{diag}\left(\overline{\mathbf{K}}\right) = \left(\omega_{1,0}^2\ \omega_{2,0}^2\ \ldots\ \omega_{n_p,0}^2\right)$.

Therefore, defining the modal state vector $\overline{\mathbf{x}} = \left(\overline{\mathbf{q}}^T\ \dot{\overline{\mathbf{q}}}^T\right)^T \in \mathbb{R}^{n_s}$, Eq. (21.16) can be reformulated in the form of the two first-order relations

$$\begin{cases} \dot{\overline{\mathbf{x}}}(t) = \overline{\mathbf{A}}\,\overline{\mathbf{x}}(t) + \overline{\mathbf{B}}\,\mathbf{e}(t) \\ \mathbf{q}(t) = \overline{\mathbf{C}}\,\overline{\mathbf{x}}(t) + \overline{\mathbf{D}}\,\mathbf{e}(t) \end{cases} \tag{21.17}$$

where the state, extended input, output and direct feedthrough matrices in modal space are given by

$$\overline{\mathbf{A}} = \begin{pmatrix} \mathbf{0}^{n_p \times n_p} & \mathbf{I}^{n_p \times n_p} \\ -\overline{\mathbf{K}} & -\overline{\mathbf{C}}_v \end{pmatrix};\ \overline{\mathbf{B}} = \begin{pmatrix} \mathbf{0}^{n_p \times n_p} & \mathbf{0}^{n_p \times n_p} & \mathbf{0}^{n_p \times n_p} & \ldots & \mathbf{0}^{n_p \times n_p} \\ \mathbf{\Phi}^T & -c_1\,\mathbf{\Phi}^T & -c_2\,\mathbf{\Phi}^T & \ldots & -c_s\,\mathbf{\Phi}^T \end{pmatrix}$$

$$\overline{\mathbf{C}} = \begin{pmatrix} \mathbf{\Phi} & \mathbf{0}^{n_p \times n_p} \end{pmatrix};\ \overline{\mathbf{D}} = \mathbf{0}^{n_p \times (s+1)\,n_p}. \tag{21.18}$$

Undamped state-space model equations in modal space can finally be constructed by imposing zero damping in Eq. (21.18), that is $\overline{\mathbf{C}}_v = \mathbf{0}^{n_p \times n_p}$. The nonlinear coefficients c_a, the undamped frequencies $\omega_{i,0}$ and the scaled mode shape matrix $\mathbf{\Phi}$ in Eq. (21.18) are obtained via Eqs. (21.10), (21.11) and (21.14), respectively.

Note that, in a real measurement setup, the structure of interest is tested over a limited frequency interval, typically encompassing a few tens of modes depending on the input bandwidth and the sampling frequency. Assuming that $m < n_p$ linear modes are excited and identified given input and output data, this results into the truncation of the diagonal of $\overline{\mathbf{K}}$ such that $\text{diag}\left(\overline{\mathbf{K}}\right) = \left(\omega_{1,0}^2\ \omega_{2,0}^2\ \ldots\ \omega_{m,0}^2\right)$. The dimension of the scaled mode shape matrix $\mathbf{\Phi}$ is similarly truncated to m columns.

21.3.2 Computation of the Individual NNMS in the State Space Using Numerical Continuation

According to their definition given in Sect. 21.2 in the conservative case, NNMs can be sought numerically as periodic solutions of the governing nonlinear equations of motion, i.e. Eq. (21.17) in the proposed identification methodology. To this end, a two-step algorithm is exploited in the present study combining shooting and pseudo-arclength continuation. This section provides a succinct description of the two techniques. The interested reader is referred to [25] for more in-depth comments.

Shooting is a popular numerical technique for solving the two-point boundary-value problem associated with the periodicity condition

$$\mathbf{S}(\mathrm{T}, \overline{\mathbf{x}}_{p0}) \equiv \overline{\mathbf{x}}_p(\mathrm{T}, \overline{\mathbf{x}}_{p0}) - \overline{\mathbf{x}}_{p0} = \mathbf{0} \tag{21.19}$$

where $\mathbf{S}(\mathrm{T}, \overline{\mathbf{x}}_{p0})$ is called the shooting function. It expresses the difference between the final state at time T of the system $\overline{\mathbf{x}}_p(\mathrm{T}, \overline{\mathbf{x}}_{p0})$ and the initial state of the system $\overline{\mathbf{x}}_{p0}$. A solution $\overline{\mathbf{x}}_p(t, \overline{\mathbf{x}}_{p0})$ is periodic if

$$\overline{\mathbf{x}}_p(t, \overline{\mathbf{x}}_{p0}) = \overline{\mathbf{x}}_p(t + \mathrm{T}, \overline{\mathbf{x}}_{p0}) \tag{21.20}$$

where T is the minimal period. In a shooting algorithm, the period T and the initial conditions $\overline{\mathbf{x}}_{p0}$ realizing a periodic motion are found iteratively. More specifically, direct numerical integration is carried out to obtain an initial guess of the periodic solution, which is corrected by means of a Newton-Raphson procedure to converge to the actual solution. In this work, time integration is performed using a fifth-order Runge-Kutta scheme with an automatic selection of the time step.

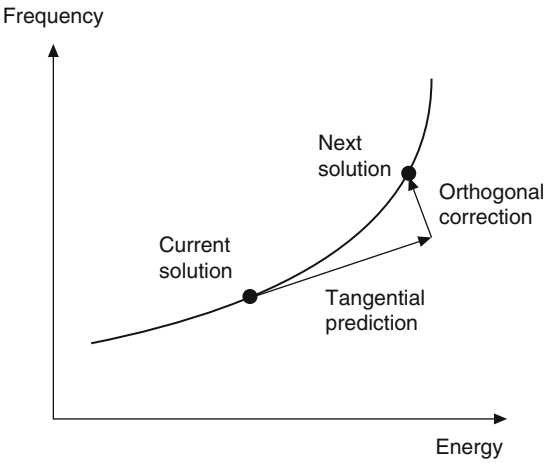

Fig. 21.5 Computation of a family of periodic solutions using a pseudo-arclength continuation scheme including prediction and correction steps

One notes that the truncation of $\overline{\mathbf{K}}$ and $\mathbf{\Phi}$ in Eq. (21.18) according to the m identified linear modes discards high-frequency modes in the experimental model. This allows a reasonably large time step to be considered during time integration, which may substantially reduce the computational burden.

Another important remark in the resolution of the boundary-value problem formulated in Eq. (21.19) is that the phase of the periodic solutions is not unique. If $\bar{\mathbf{x}}_p(t)$ is a solution of Eq. (21.17), then $\bar{\mathbf{x}}_p(t + \Delta t)$ is geometrically the same solution in state space for any Δt. Hence, an additional condition $s(\bar{\mathbf{x}}_{p0}) = 0$, termed phase condition, is specified to remove the arbitrariness of the initial conditions. Following the approach in [25], the modal velocities $\dot{\bar{\mathbf{q}}}_0$ are set equal to zero. In summary, an isolated NNM motion is computed by solving the augmented two-point boundary-value problem defined by the two relations

$$\begin{aligned} \mathbf{S}(\mathrm{T}, \bar{\mathbf{x}}_{p0}) &= 0 \\ s(\bar{\mathbf{x}}_{p0}) &= 0. \end{aligned} \tag{21.21}$$

To obtain the family of periodic solutions that describe the considered NNM, shooting is combined with a pseudo-arclength continuation technique. Starting from a known periodic solution, continuation proceeds in two steps, namely a prediction and a correction, as illustrated in Fig. 21.5. In the prediction step, a guess of the next periodic solution along the NNM branch is generated in the direction of the tangent vector to the branch at the current solution. Next, the prediction is corrected using a shooting procedure, forcing the variations of the period and the initial conditions to be orthogonal to the prediction direction. Note that this shooting-continuation algorithm was used to construct Fig. 21.1.

21.4 Numerical Demonstration Using a Cantilever Beam Possessing a Cubic Nonlinearity

In this section, the developed methodology for the identification of NNMs is demonstrated based on numerical experiments carried out on the nonlinear beam structure proposed as a benchmark during the European COST Action F3 [41]. This structure consists of a main cantilever beam whose free end is connected to a thin beam clamped on the other side. The thin beam can exhibit geometrically nonlinear behavior for sufficiently large displacements. It should be noted that the same case study was investigated to demonstrate the nonlinear phase resonance method developed in [31, 32].

The finite element model of the structure considered in this work is represented in Fig. 21.6 and is identical to the experimentally-updated model in [32]. It comprises 14 two-dimensional beam elements for the main beam and three elements for the thin beam. As shown in [35, 42], the nonlinear dynamics induced by the thin beam can be modeled through a grounded cubic spring associated with a coefficient c_1, and positioned at the connection between the two beams. The geometrical and mechanical properties of the structure are listed in Tables 21.1 and 21.2, respectively.

Numerical experiments were conducted by direct time integration using a nonlinear Newmark scheme. To this end, a linear damping matrix $\mathbf{C}_v$ was introduced in the model via a proportionality relation with the mass and stiffness matrices, i.e.

$$\mathbf{C}_v = \alpha\mathbf{K} + \beta\mathbf{M}, \tag{21.22}$$

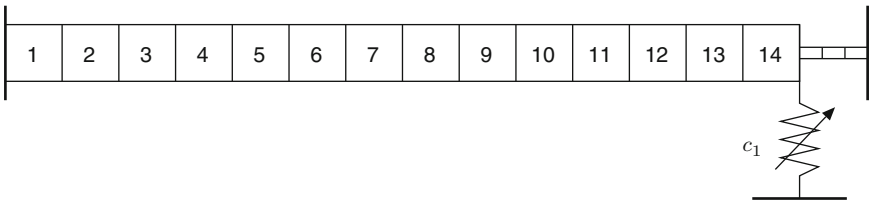

Fig. 21.6 Finite element model of the nonlinear beam

Table 21.1 Geometrical properties of the nonlinear beam

	Length (m)	Width (mm)	Thickness (mm)
Main beam	0.7	14	14
Thin beam	0.04	14	0.5

Table 21.2 Mechanical properties of the nonlinear beam

Young's modulus (N/m^2)	Density (kg/m^3)	Nonlinear coefficient c_1 (N/m^3)
$2.05\ 10^{11}$	7,800	$8\ 10^9$

Table 21.3 Linear natural frequencies ω_0 and damping ratios ϵ of the first three bending modes of the nonlinear beam

Mode	Natural frequency ω_0 (Hz)	Damping ratio ε (%)
1	31.28	1.28
2	143.64	0.29
3	397.87	0.14

with $\alpha = 3\ 10^{-7}$ and $\beta = 5$. The resulting linear natural frequencies and damping ratios of the first three bending modes of the beam structure are given in Table 21.3. The sampling frequency during time simulation was set to 60,000 Hz to ensure the accuracy of the integration. Synthetic time series were then decimated down to 3,000 Hz for practical use, considering low-pass filtering to avoid aliasing.

21.4.1 Identification Using the FNSI Method Under a Multisine Excitation

According to the scheme in Fig. 21.3, the proposed testing procedure starts with the application of a broadband excitation signal to the nonlinear beam structure. Note that the FNSI method can address classical random excitations, including Gaussian noise, periodic random, burst random and pseudo random signals. Stepped-sine and swept-sine excitations are not applicable because of the inability of the FNSI method to handle nonstationary signals, i.e. signals with time-varying frequency content [35]. One opts herein for pseudo random signals, also known as random phase multisine signals. A random phase multisine is a periodic random signal with a user-controlled amplitude spectrum, and a random phase spectrum drawn from a uniform distribution. If an integer number of periods is measured, the amplitude spectrum is perfectly realized, unlike Gaussian noise. One of the other main advantages of a multisine is that its periodic nature can be utilized to separate the transient and the steady-state responses of the system. This, in turn, eliminates the systematic errors due to leakage in the identification.

A multisine excitation with a flat amplitude spectrum and a root-mean-squared (RMS) amplitude of 15 N was applied vertically to node 4 of the structure. The excited band spans the 5–500 Hz interval to encompass the three linear modes of interest. The response of the nonlinear beam was simulated over ten periods of 32,768 samples each, nine periods of which were discarded to achieve steady-state conditions. Figure 21.7a, b shows the amplitude spectrum and the phase spectrum of one period of the considered multisine input, respectively. The complete signal containing ten periods is depicted in Fig. 21.7c, where one specific period is highlighted in gray. Finally, the decay of the transient response measured at the main beam tip is illustrated in logarithmic scaling in Fig. 21.7d. The latter plot was obtained by subtracting from the entire signal the last period of measurement, assumed to be in steady state.

21.4.1.1 Selection of the Nonlinear Basis Functions

The application of the FNSI method to measured data requires the selection of appropriate basis functions $\mathbf{h}_a(\mathbf{q}(t), \dot{\mathbf{q}}(t))$ to describe the nonlinearity in the system. This task, referred to as the characterization of nonlinearity, is in general challenging because of the various sources of nonlinear behavior that may exist in engineering structures, and the plethora of

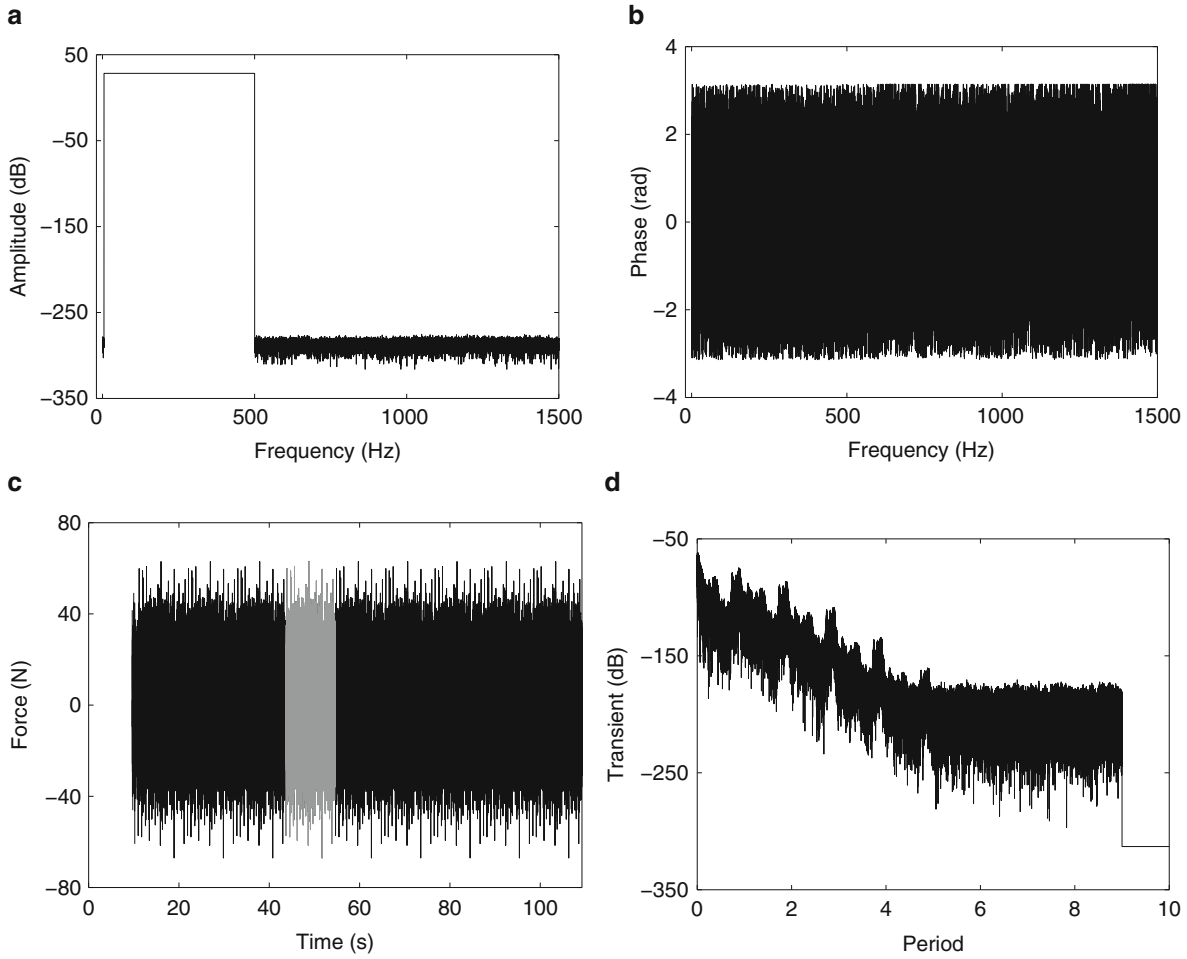

Fig. 21.7 Random phase multisine excitation signal. (**a**, **b**) Amplitude and phase spectrum of a single period; (**c**) complete signal containing ten periods with one specific period highlighted in *gray*; (**d**) decay of the transient response at the main beam tip in logarithmic scaling

dynamic phenomena they may cause [43]. One possible approach to discriminate between different candidate nonlinearity models is the use of a subspace identification error criterion, as detailed in [36]. Characterization may also be partly bypassed by resorting to mathematical functionals capable of representing a vast class of nonlinearities, such as high-order polynomials [44], neural networks [45] or splines [37]. In this study, we assume the knowledge of nonlinear functional form associated with the thin beam, namely a cubic restoring force in displacement.

21.4.1.2 Selection of the Model Order

The order of the state-space model derived using the FNSI method is equal to twice the number of linear modes activated in the measured data [35]. This order is conveniently estimated using a stabilization diagram, similarly to the current practice in linear system identification. Figure 21.8 charts the stabilization of the natural frequencies, damping ratios and mode shapes of the structure computed at 15 N RMS for model orders up to 20. In this diagram, the modal assurance criterion (MAC) is utilized to quantify the correspondence between mode shapes at different orders. Figure 21.8 shows full stabilization of the first three modes of the structure at order 6. Note that full stabilization symbols only appear at order 8. However, since this is tested between successive model orders taking as reference the lowest order, equal stabilization is also achieved at order 6, which is therefore selected to avoid spurious poles.

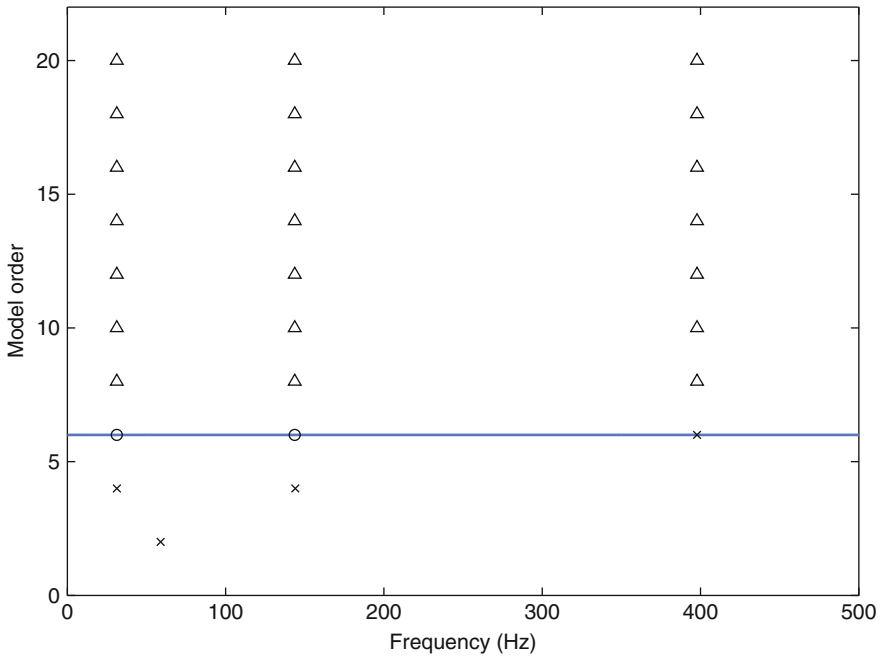

Fig. 21.8 Stabilization diagram. *Cross*: stabilization in natural frequency; *circle*: extra stabilization in MAC; *triangle*: full stabilization. Stabilization thresholds in natural frequency, damping ratio and MAC are 1 %, 5 % and 0.98, respectively. The *blue line* indicates the selected order (Color figure online)

Table 21.4 Relative errors on the estimated natural frequencies and damping ratios (in %) and diagonal MAC values of the first three modes of the beam computed at order 6

Mode	Error on ω_0 (%)	Error on ε (%)	MAC
1	0.0004	−0.0175	1.00
2	−0.0020	0.0180	1.00
3	−0.0144	−0.0461	1.00

21.4.1.3 Estimation of the Underlying Linear Properties

Table 21.4 lists the relative errors on the estimated natural frequencies and damping ratios together with the diagonal MAC values. The results in this table demonstrate the ability of the FNSI method to recover accurately the modal properties of the underlying linear structure from nonlinear data. The overall quality of the linear parameter estimates is confirmed in Fig. 21.9a, b, where the exact FRF at the main beam tip is compared with the corresponding FRF synthesized using the FNSI method at 15 N RMS for the first and second modes of the structure, respectively. The FRFs calculated at high level using a linear estimator are also visible in the two plots, and highlight the importance of the nonlinear distortions affecting the beam dynamics. Note that, since the considered nonlinearity is a function of the displacement at the main beam tip, the distortions appearing around the first mode are more substantial. For the same reason, the third bending mode is only marginally impacted at 15 N RMS, and is hence not depicted.

21.4.1.4 Estimation of the Nonlinear Coefficient

The nonlinear coefficient c_1 is estimated using Eq. (21.10) and is consequently a spectral quantity, i.e. it is complex-valued and frequency-dependent. This is an attractive property because the significance of its frequency variations and imaginary part turns out to be particularly convenient to assess the quality of the identification. Figure 21.10a, b depicts the real and imaginary parts of the coefficient, respectively. The real part shows almost no dependence upon frequency, and the imaginary part is more than three orders of magnitude smaller (see Table 21.5). Table 21.5 gives the averaged value of the nonlinear coefficient, the relative error and the ratio between its real and imaginary parts in logarithmic scaling. This table reveals the excellent agreement between the identified and exact coefficients.

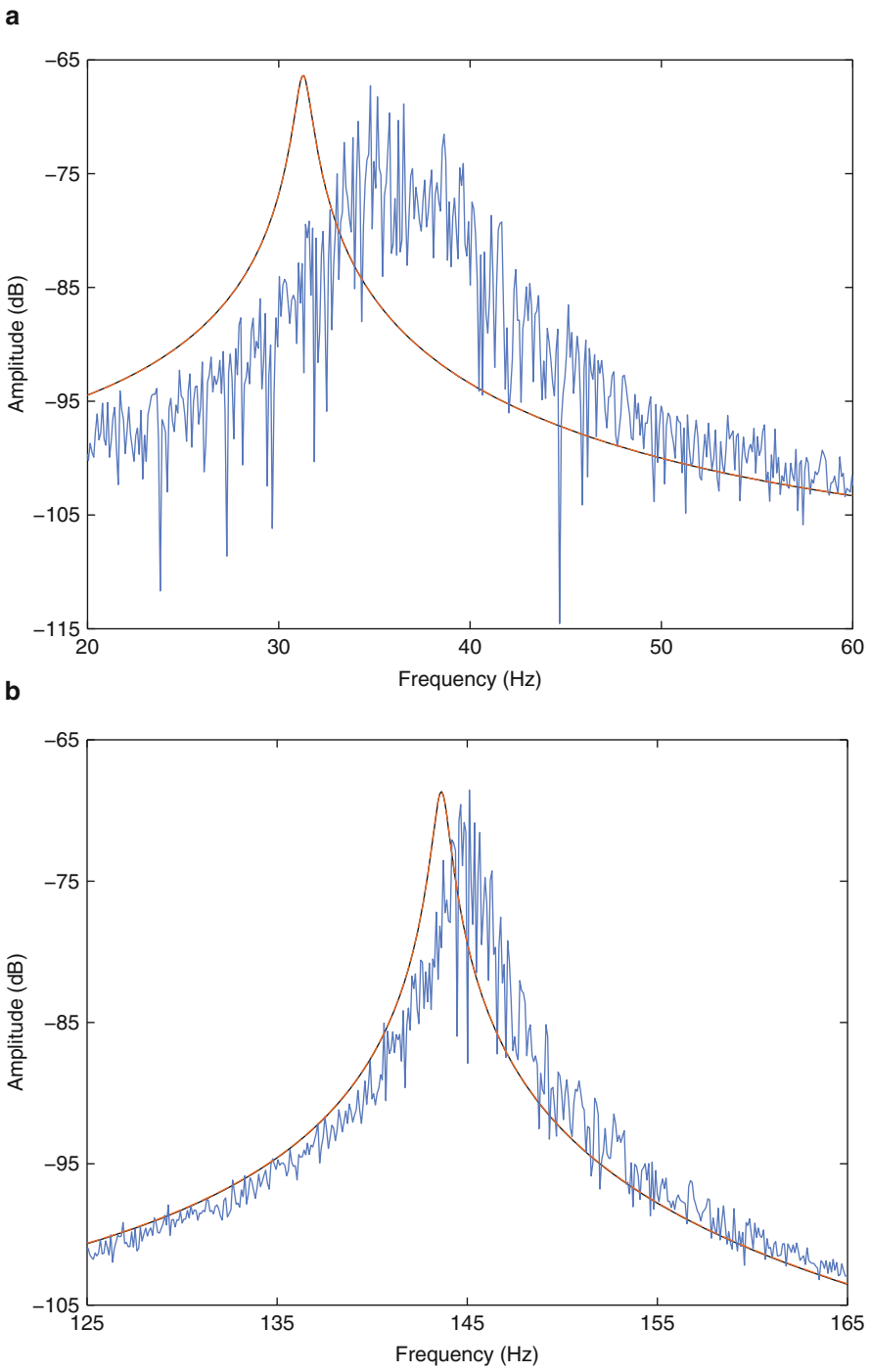

Fig. 21.9 Comparison between the exact linear FRF at the main beam tip (in *black*) and the corresponding curve synthesized using the FNSI method at high level (in *orange*), i.e. at 15 N RMS. The FRF calculated using a linear estimator at high level is also superposed (in *blue*). (**a**) First mode; (**b**) second mode (Color figure online)

21.4.1.5 Removal of Damping Terms

Damping terms are finally removed from the identified nonlinear state-space model $(\mathbf{A}, \mathbf{B}, \mathbf{C}, \mathbf{D})$ following the constructive procedure of Sect. 21.3.1.4. The resulting undamped model equations form the basis of the subsequent computation of NNMs using numerical techniques.

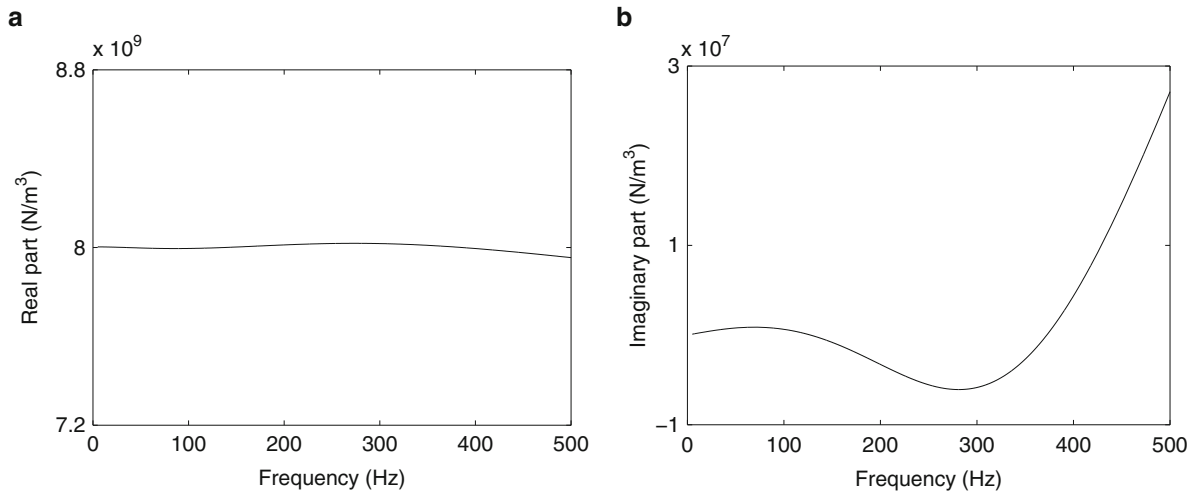

Fig. 21.10 Complex and frequency-dependent estimate of the nonlinear coefficient c_1. (**a**) Real part; (**b**) imaginary part

Table 21.5 Estimate of the nonlinear coefficient c_1

Exact value (GN/m^3)	Real part (GN/m^3)	Error (%)	Log_{10} (real/imag.)
8	8.0005	0.0062	3.72

Real part averaged over 5–500 Hz, relative error (in %) and ratio between the real and imaginary parts (in logarithmic scaling)

21.4.2 Computation of the First Two NNMS Using Continuation

In this section, the algorithm of Sect. 21.3.2 is applied to the undamped model equations identified in Sect. 21.4.1 to compute the first two NNMs of the beam structure. Note that the third mode is not analyzed herein as it involves virtually no nonlinear distortions. Figure 21.11 shows the evolution of the frequency of the first bending mode of the structure as a function of the amplitude of the motion evaluated at the main beam tip. The use of a displacement amplitude as horizontal axis in this plot is justified by the absence of direct access to the total conserved energy associated with the considered mode in experimental conditions [32]. The identified frequency-amplitude curve depicted in orange in Fig. 21.11 is seen to closely match with the exact NNM presented in black, proving the accuracy of the proposed identification methodology. This is confirmed through the comparison between the exact and identified modal shapes inserted in Fig. 21.11 at four specific amplitude levels, namely 0.2, 0.4, 0.6 and 0.8 mm. Similar conclusions are drawn from the quality of the identification of the second mode of the nonlinear beam plotted in Fig. 21.13.

It should be underlined that the results in Fig. 21.11 demonstrate the validity of the NNM identification methodology for strongly nonlinear regimes of motion. Specifically, a hardening of almost 8 Hz of the natural frequency is found to be accurately captured in this plot. This substantial frequency shift corresponds to an amplitude of motion of 1 mm at the main beam tip, which is twice the thickness of the thin beam. The importance of nonlinearity in the beam dynamics is well evidenced in Fig. 21.12a, b, where the first NNM of the structure is represented in the configuration space for amplitudes of 0.2 and 0.8 mm, respectively. The configuration space is spanned in this figure by the displacements measured at nodes 4 and 14, i.e. at the driving point and the main beam tip, respectively. One observes that, at low amplitude level in Fig. 21.12a, the NNM is a straight line, whereas it corresponds to a curved line for high amplitudes in Fig. 21.12b, revealing the appearance of harmonics in the time series. A similar analysis is achieved in Fig. 21.14a, b for the second NNM of the beam. These two graphs show that, owing to the displacement nature of the involved nonlinearity, higher-frequency modes are less impacted by harmonic distortions, and translate into straight lines in configuration space even for large amplitudes of motion.

One finally points out that the amplitude axes in Figs. 21.11 and 21.13 were arbitrarily limited to 1 mm. This choice relates to the validity range of the amplitude-dependent periodic solutions calculated based on an experimental model derived using broadband data. In this study, the amplitude interval over which the continuation was performed was merely selected by observing that the maximum amplitude of displacement recorded in Sect. 21.4.1 at the main beam tip under multisine forcing was of the order of 1 mm. Moreover, the frequency shifts noticed in Fig. 21.9a, b through the blue curves are seen to be consistent with the extent of the frequency axes in Figs. 21.11 and 21.13. However, a rigorous evaluation of the validity ranges of identified frequency-amplitude plots remains an open question and should deserve more investigation.

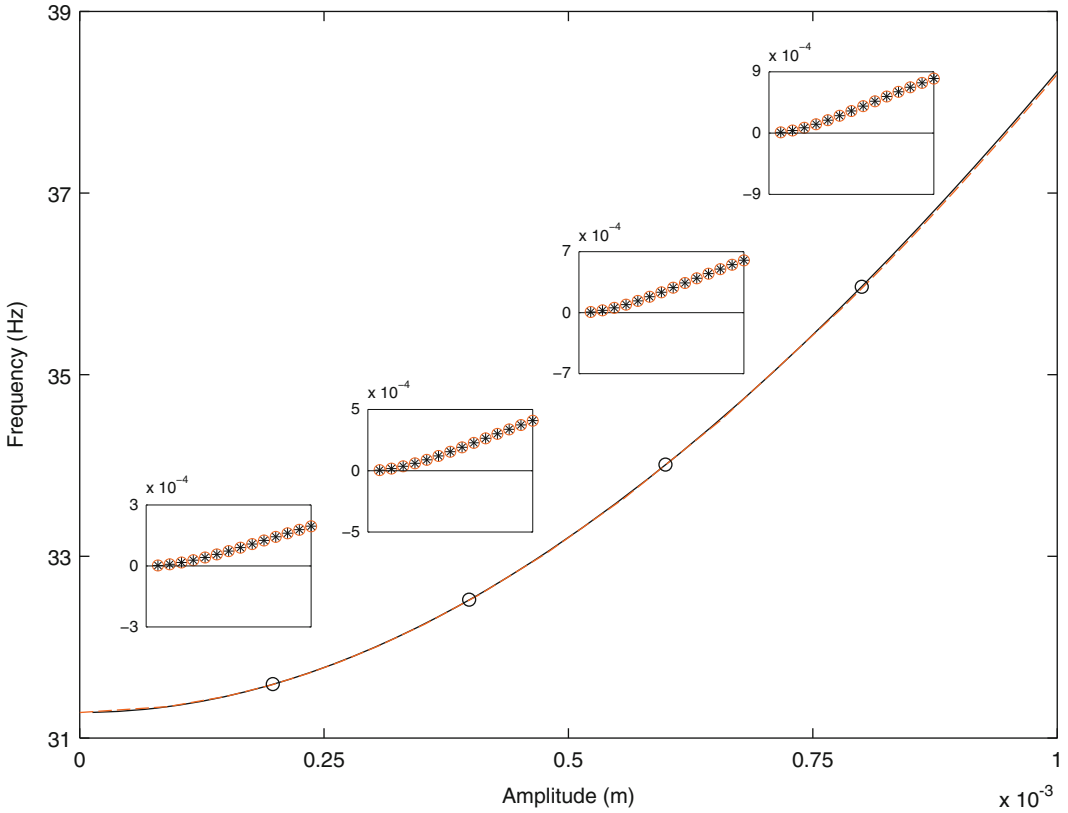

Fig. 21.11 Comparison between the theoretical (in *black*) and identified (in *orange*) frequency-amplitude evolution of the first NNM of the nonlinear beam. The NNM shapes (displacement amplitudes of the main beam) at four amplitude levels, namely 0.2, 0.4, 0.6 and 0.8 mm, are *inset* (Color figure online)

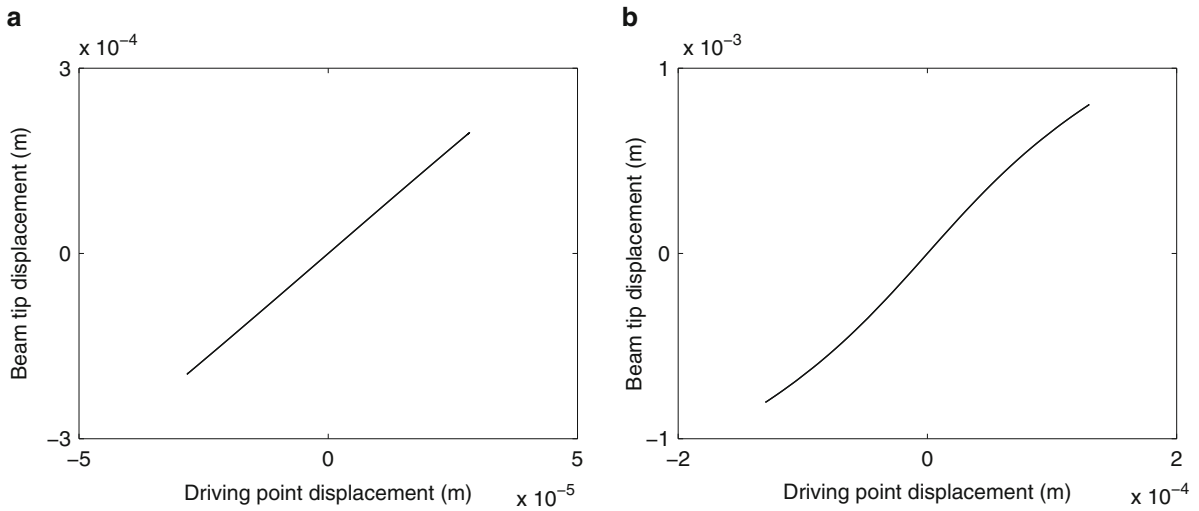

Fig. 21.12 First NNM of the nonlinear beam represented in configuration space at two amplitude levels. The configuration space is constructed using the displacements measured at the driving point and the main beam tip. (**a**) 0.2 mm ; (**b**) 0.8 mm

21.5 Comparison with NNMs Identified Using Nonlinear Phase Resonance

This final section is dedicated to a comparison between the identification methodology proposed in this work, which can be seen as a generalization of the classical linear phase separation testing techniques, and the nonlinear phase resonance approach of [31]. As explained in Sect. 21.2 and depicted in Fig. 21.2, the first step of the nonlinear phase resonance testing

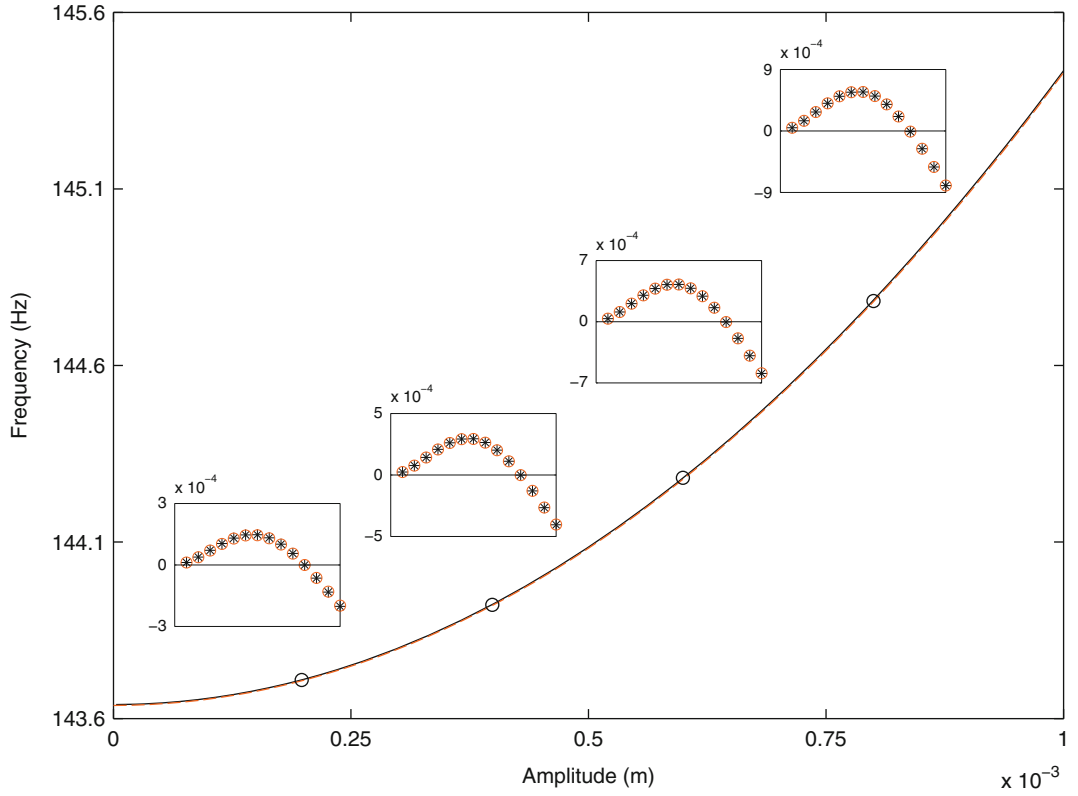

Fig. 21.13 Comparison between the theoretical (in *black*) and identified (in *orange*) frequency-amplitude evolution of the second NNM of the nonlinear beam. The NNM shapes (displacement amplitudes of the main beam) at four amplitude levels, namely 0.2, 0.4, 0.6 and 0.8 mm, are *inset* (Color figure online)

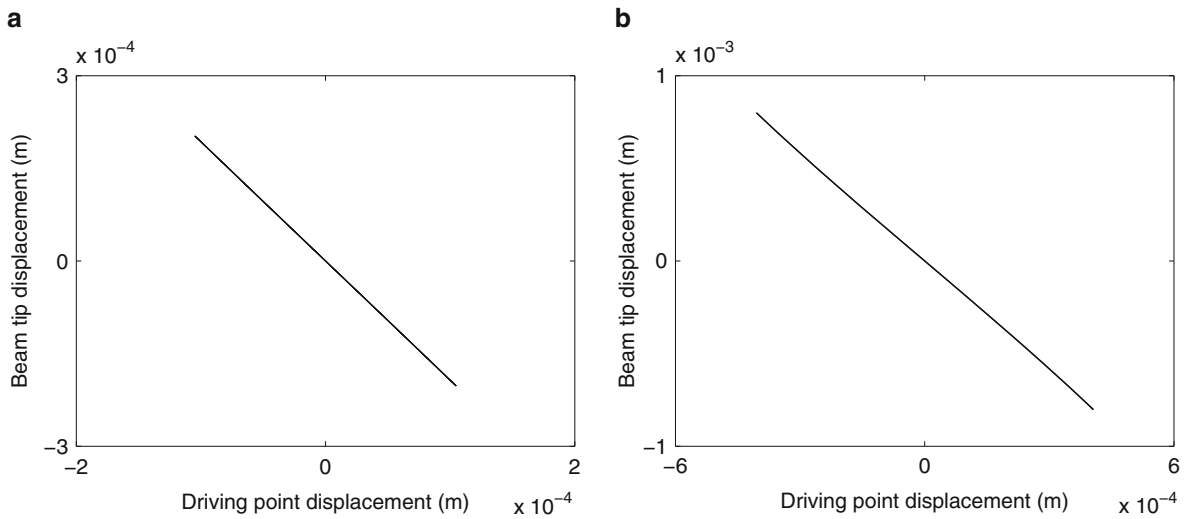

Fig. 21.14 Second NNM of the nonlinear beam represented in configuration space at two amplitude levels. The configuration space is constructed using the displacements measured at the driving point and the main beam tip. (**a**) 0.2 mm; (**b**) 0.8 mm

procedure is the appropriation of the NNM of interest. This is realized by tuning the frequency of a stepped-sine excitation so as to induce of a single-NNM motion of the system. This step is facilitated by a generalized phase lag quadrature criterion, which can be translated into a force appropriation indicator equal to 1 at resonance [32]. NNM appropriation is illustrated in Fig. 21.15a, b in the case of the first mode of the nonlinear beam. The excitation is a 4 N sine signal applied to node 4 of the structure. Figure 21.15a plots the evolution of the appropriation indicator with respect to the forcing frequency. It reaches a

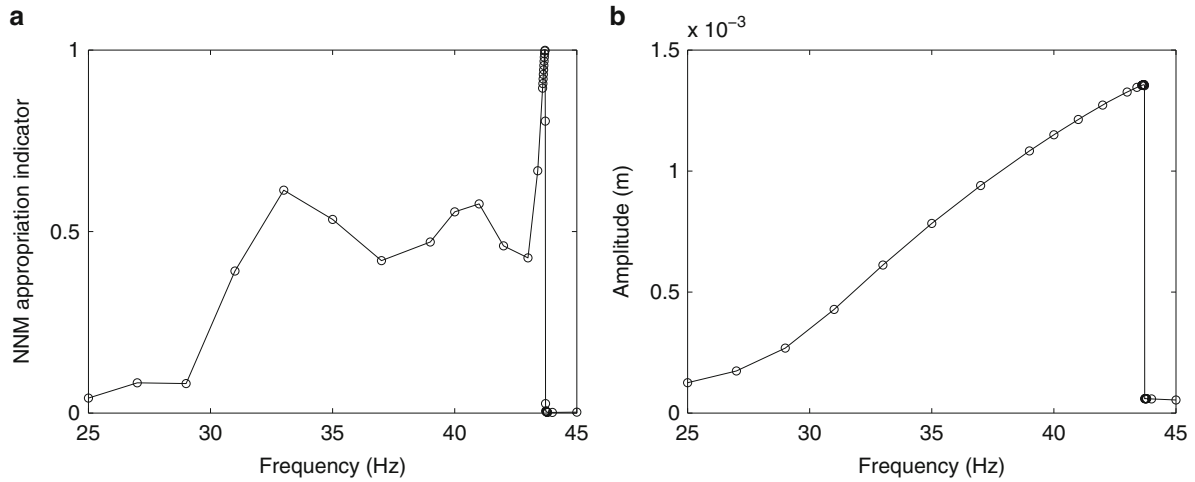

Fig. 21.15 Appropriation of the first NNM of the beam structure in the nonlinear phase resonance method. (**a**) NNM appropriation indicator; (**b**) amplitude of the response at the main beam tip

value equal to 1 for a frequency close to 43.7 Hz. The corresponding amplitude of the forced response measured at the main beam tip is depicted in Fig. 21.15b. This graph shows the distorted frequency response of the first mode and the sudden jump occurring as soon as resonance is passed.

When the considered NNM is appropriated, the second step of the nonlinear phase resonance procedure is to turn off the excitation in order to observe the free decay of the system along the NNM branch. A time-frequency analysis of the decaying time response is then carried out to extract the frequency-energy dependence of the mode. This is achieved in Fig. 21.16 where the wavelet transform of the displacement measured at beam tip during the free decay is represented. The ridge of the wavelet, i.e. the locus of maximum amplitude with respect to frequency, is presented as a black line, and is seen to closely coincide with the NNM identified in the previous section and plotted in orange. The comparable accuracy of the phase separation and phase resonance approaches is confirmed by the modal shapes superposed at four amplitude levels in Fig. 21.16. The results in this figure, together with the analysis of the second NNM appropriation reported in Figs. 21.17 and 21.18, clearly confirm the claimed accuracy of the NNM identification methodology developed in the present paper. In summary, Table 21.6 lists the strengths and limitations of the two methodologies.

21.6 Conclusion

The present paper introduced a methodology capable of extracting experimentally the nonlinear normal modes (NNMs) of vibrating systems from measurements collected under broadband forcing. This is the first methodology suffering from no restriction regarding the strength of the nonlinearities and the modal coupling. It relies on the joint utilization of nonlinear system identification and numerical continuation of periodic solutions. The methodology can be viewed as the ideal complement to a previously-developed approach for the identification of NNMs from sine data. Together, they provide rigorous generalizations of the testing procedures routinely exploited for experimental modal analysis of linear engineering structures.

Further work will focus on the experimental demonstration of the methodology proposed herein. In this context, the use of splines will be investigated in order to bypass the a priori assumption of a mathematical model for the nonlinearities. Another research direction is the extension of the methodology to systems with damping nonlinearities through the direct computation of damped NNMs based on the experimentally-derived state-space model.

Acknowledgements The author J.P. Noël is a Postdoctoral Researcher of the *Fonds de la Recherche Scientifique – FNRS* which is gratefully acknowledged. The author L. Renson is a Marie-Curie COFUND Postdoctoral Fellow of the University of Liège, co-funded by the European Union. The authors C. Grappasonni and G. Kerschen would like to acknowledge the financial support of the European Union (ERC Starting Grant NoVib 307265).

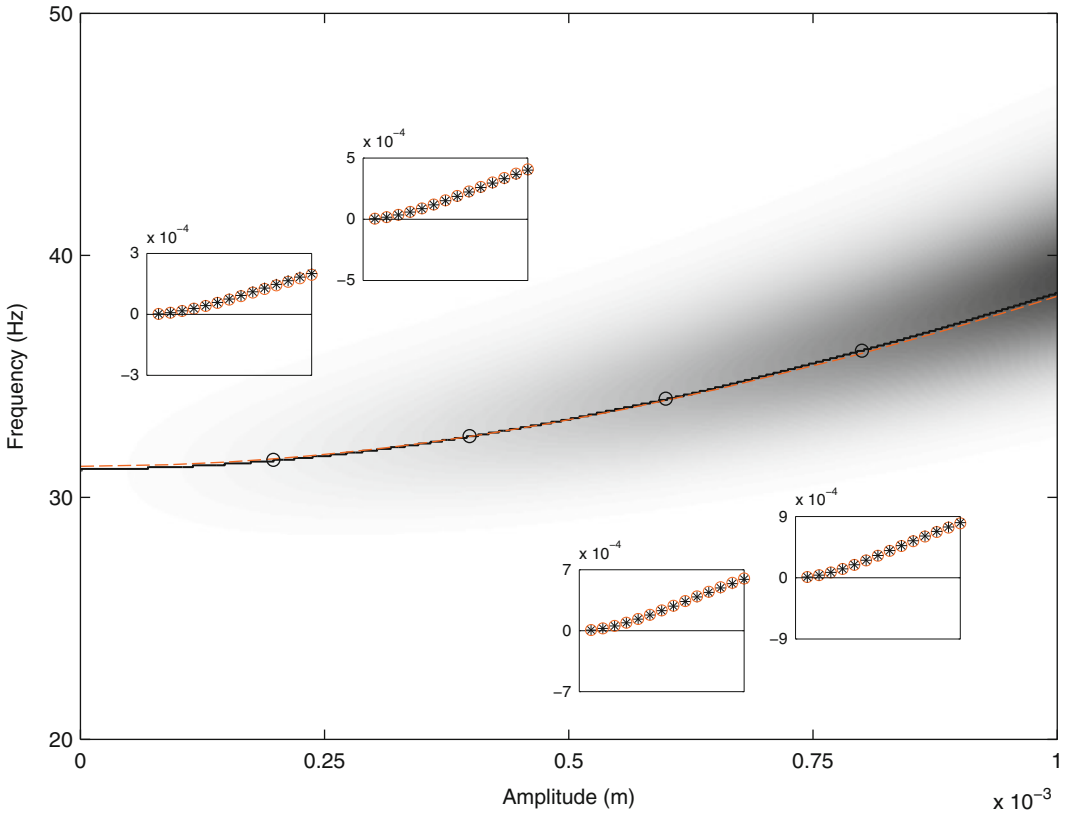

Fig. 21.16 Decay along the first NNM branch calculated using time-frequency analysis (in *black*) and corresponding NNM obtained in Sect. 21.4.2 using the proposed identification methodology (in *orange*). The NNM shapes (displacement amplitudes of the main beam) at four amplitude levels, namely 0.2, 0.4, 0.6 and 0.8 mm, are *inset* (Color figure online)

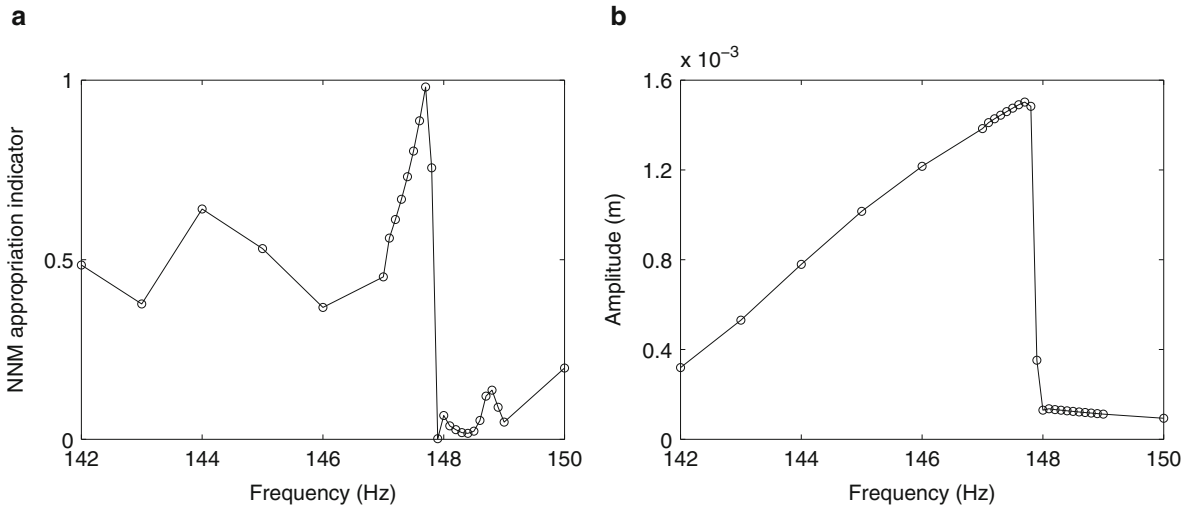

Fig. 21.17 Appropriation of the second NNM of the beam structure in the nonlinear phase resonance method. (**a**) NNM appropriation indicator; (**b**) amplitude of the response at the main beam tip

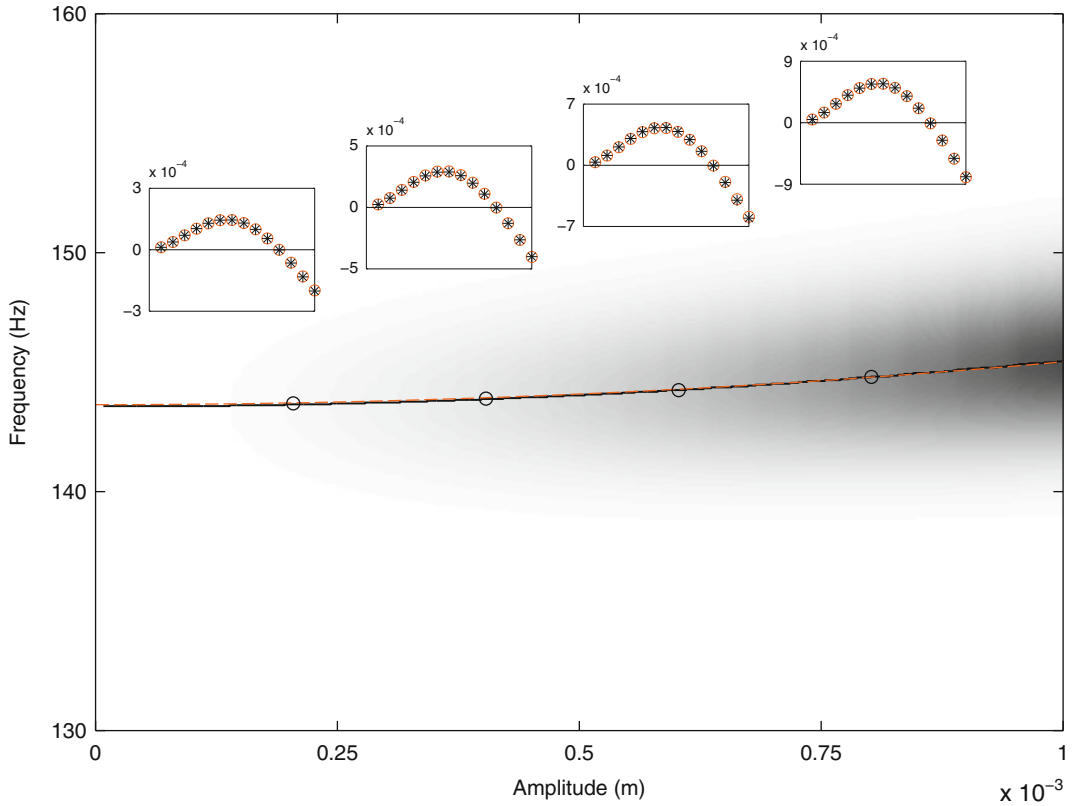

Fig. 21.18 Decay along the second NNM branch calculated using time-frequency analysis (in *black*) and corresponding NNM obtained in Sect. 21.4.2 using the proposed identification methodology (in *orange*). The NNM shapes (displacement amplitudes of the main beam) at four amplitude levels, namely 0.2, 0.4, 0.6 and 0.8 mm, are *inset* (Color figure online)

Table 21.6 Comparison of the strengths and limitations of the two methodologies

Nonlinear phase separation method	Nonlinear phase resonance method
Fast (multiple NNMs simultaneously)	Time-consuming (one NNM at a time, and difficulty to reach resonance)
Need of an experimental model	Model-free
Classical random excitation can be utilized	Multi-harmonic forcing is needed
Nonlinear components must be instrumented on both sides	Multiple shakers are needed and must be turned off
Nonlinearity characterization is required	Limited information needed about the nonlinearities
Damping in the experimental model must be removed	Undamped NNMs are directly obtained

References

1. Ewins D (2006) A future for experimental structural dynamics. In: Proceedings of the international conference on noise and vibration engineering (ISMA), Leuven, Belgium
2. Peeters B, Climent H, de Diego R, de Alba J, Ahlquist J, Carreño J, Hendricx W, Rega A, Garcia G, Deweer J, Debille J (2008) Modern solutions for ground vibration testing of large aircraft. In: Proceedings of the 26th international modal analysis conference (IMAC), Orlando, FL
3. Göge D, Böswald M, Füllekrug U, Lubrina P (2007) Ground vibration testing of large aircraft: state of the art and future perspectives. In: Proceedings of the 25th international modal analysis conference (IMAC), Orlando, FL
4. Grillenbeck A, Dillinger S (2011) Reliability of experimental modal data determined on large spaceflight structures. In: Proceedings of the 29th international modal analysis conference (IMAC), Jacksonville, FL
5. Wright J, Cooper J, Desforges M (1999) Normal-mode force appropriation - theory and application. Mech Syst Signal Process 13:217–240
6. Peeters B, Van der Auweraer H, Guillaume P, Leuridan, J (2004) The PolyMAX frequency-domain method: a new standard for modal parameter estimation? Shock Vib 11(3–4):395–409
7. Van Overschee P, De Moor B (1996) Subspace identification for linear systems: theory, implementation and applications. Kluwer Academic Publishers, Dordrecht
8. Atkins P, Wright J, Worden K (2000) An extension of force appropriation to the identification of non-linear multi-degree of freedom systems. J Sound Vib 237:23–43
9. Platten M, Wright JR, Dimitriadis G, Cooper J (2009) Identification of multi-degree of freedom non-linear systems using an extended modal space model. Mech Syst Signal Process 23:8–29
10. Poon C, Chang C (2007) Identification of nonlinear elastic structures using empirical mode decomposition and nonlinear normal modes. Smart Struct Syst 3:423–437
11. Vakakis A, Bergman L, McFarland D, Lee Y, Kurt M (2011) Current efforts towards a non-linear system identification methodology of broad applicability. Proc Inst Mech Eng C J Mech Eng Sci 225:2497–2515
12. Eriten M, Kurt M, Luo G, Vakakis A, McFarland D, Bergman L (2013) Nonlinear system identification of frictional effects in a beam with bolted connection. Mech Syst Signal Process 39:245–264
13. Pai P (2011) Time-frequency characterization of nonlinear normal modes and challenges in nonlinearity identification of dynamical systems. Mech Syst Signal Process 25:2358–2374
14. Worden K, Green P (2014) A machine learning approach to nonlinear modal analysis. In: Proceedings of the 32nd international modal analysis conference (IMAC), Orlando, FL
15. Gibert C (2003) Fitting measured frequency response functions using non-linear modes. Mech Syst Signal Process 17:211–218
16. Chong Y, Imregun M (2001) Development and application of a nonlinear modal analysis technique for MDOF systems. J Vib Control 7: 167–179
17. Rosenberg R (1962) The normal modes of nonlinear n-degree-of-freedom systems. J Appl Mech 29:7–14
18. Rosenberg R (1966) On nonlinear vibrations of systems with many degrees of freedom. Adv Appl Mech 9:217–240
19. Shaw S, Pierre C (1993) Normal modes for non-linear vibratory systems. J Sound Vib 164(1):85–124
20. Vakakis A, Manevitch L, Mlkhlin Y, Pilipchuk V, Zevin A (1996) Normal modes and localization in nonlinear systems. Wiley, New York
21. Lacarbonara W, Camillacci R (2004) Nonlinear normal modes of structural systems via asymptotic approach. Int J Solids Struct 41:5565–5594
22. Touzé C, Amabili M (2006) Nonlinear normal modes for damped geometrically nonlinear systems: application to reduced-order modelling of harmonically forced structures. J Sound Vib 298:958–981
23. Kerschen G, Peeters M, Golinval J, Vakakis A (2009) Nonlinear normal modes. Part I: a useful framework for the structural dynamicist. Mech Syst Signal Process 23(1):170–194
24. Arquier R, Bellizzi S, Bouc R, Cochelin B (2006) Two methods for the computation of nonlinear modes of vibrating systems at large amplitudes. Comput Struct 84:1565–1576
25. Peeters M, Viguié R, Sérandour G, Kerschen G, Golinval J (2009) Nonlinear normal modes. Part II: toward a practical computation using numerical continuation techniques. Mech Syst Signal Process 23(1):195–216
26. Laxalde D, Thouverez F (2009) Complex non-linear modal analysis of mechanical systems: application to turbomachinery bladings with friction interfaces. J Sound Vib 322:1009–1025
27. Renson L, Deliége G, Kerschen G (2014) An effective finite-element-based method for the computation of nonlinear normal modes of nonconservative systems. Meccanica 49(8):1901–1916
28. Kerschen G, Peeters M, Golinval J, Stephan C (2013) Nonlinear modal analysis of a full-scale aircraft. J Aircr 50:1409–1419
29. Renson L, Noël J, Kerschen G (2014) Complex dynamics of a nonlinear aerospace structure: numerical continuation and normal modes. Nonlinear Dyn 79(2):1293–1309
30. Krack M, Panning-von Scheidt L, Wallaschek J (2014) A method for nonlinear modal analysis and synthesis: application to harmonically forced and self-excited mechanical systems. J Sound Vib 332(25):6798–6814
31. Peeters M, Kerschen G, Golinval J (2011) Dynamic testing of nonlinear vibrating structures using nonlinear normal modes. J Sound Vib 330:486–509
32. Peeters M, Kerschen G, Golinval J (2011) Modal testing of nonlinear vibrating structures based on nonlinear normal modes: experimental demonstration. Mech Syst Signal Process 25:1227–1247
33. Zapico-Valle J, Garcia-Dieguez M, Alonso-Camblor R (2013) Nonlinear modal identification of a steel frame. Eng Struct 56:246–259
34. Ehrhardt D, Harris R, Allen M (2014) Numerical and experimental determination of nonlinear normal modes of a circular perforated plate. In: Proceedings of the 32nd international modal analysis conference (IMAC), Orlando, FL
35. Noël J, Kerschen G (2013) Frequency-domain subspace identification for nonlinear mechanical systems. Mech Syst Signal Process 40:701–717
36. Noël J, Marchesiello S, Kerschen G (2014) Subspace-based identification of a nonlinear spacecraft in the time and frequency domains. Mech Syst Signal Process 43:217–236

37. Noël J, Kerschen G, Foltête E, Cogan S (2014) Grey-box identification of a nonlinear solar array structure using cubic splines. Int J Non-linear Mech 67:106–118
38. Adams D, Allemang R (2000) A frequency domain method for estimating the parameters of a non-linear structural dynamic model through feedback. Mech Syst Signal Process 14:637–656
39. Marchesiello S, Garibaldi L (2008) A time domain approach for identifying nonlinear vibrating structures by subspace methods. Mech Syst Signal Process 22:81–101
40. Géradin M, Rixen D (1997) Mechanical vibrations: theory and applications to structural dynamics. Wiley, Chichester
41. Thouverez F (2003) Presentation of the ECL benchmark. Mech Syst Signal Process 17(1):195–202
42. Kerschen G, Lenaerts V, Golinval J (2003) Identification of a continuous structure with a geometrical non-linearity. Part I: conditioned reverse path method. J Sound Vib 262:889–906
43. Kerschen G, Worden K, Vakakis A, Golinval J (2006) Past, present and future of nonlinear system identification in structural dynamics. Mech Syst Signal Process 20:505–592
44. Platten M, Wright J, Cooper J, Dimitriadis G (2009) Identification of a nonlinear wing structure using an extended modal model. J Aircr 46(5):1614–1626
45. Fan Y, Li C (2002) Non-linear system identification using lumped parameter models with embedded feedforward neural networks. Mech Syst Signal Process 16(2–3):357–372